Structure and Properties of Zirconia Nanoparticles from Density Functional Theory Calculations

Antonio Ruiz Puigdollers[a], Francesc Illas[b], Gianfranco Pacchioni[a,*]

[a]*Dipartimento di Scienza dei Materiali, Università di Milano-Bicocca. Via R. Cozzi 55, 20125 Milano, Italy*
[b]*Departament de Química Física and Institut de Química Teórica i Computacional (IQTCUB), Universitat de Barcelona, 08028 Barcelona, Spain.*

Abstract

The structure, stability and electronic properties of a series of zirconia nanoparticles between 1.5 and 2 nm in size, $(ZrO_{2\pm x})_n$ within the n=13 to n=85 range, have been investigated through density functional theory (DFT) based calculations. On the methodological side we compare results obtained with standard DFT functionals with the DFT+U approach and with hybrid functionals. As representative models, octahedral and truncated octahedral morphologies have been considered for the zirconia nanoparticles. Partly truncated octahedral nanoparticles with ZrO_2 stoichiometry display the highest stability. On the contrary, nanoparticles with octahedral and cuboctahedral (totally truncated octahedral) shapes are less stable due to oxygen deficiency or excess, respectively. We show that the calculated formation energies scale linearly with the average coordination number of the Zr ions, and converge to the bulk value as the particle size increases. The formation energy of a neutral oxygen vacancy in the nanoparticles has also been investigated. In comparison to the ZrO_2(101) surface of tetragonal zirconia, we found that three- and four-coordinated O atoms have similar formation energies. However, the two-coordinated O ions on the surface of the nanoparticles have considerably smaller formation energies. In this respect the effect of nanostructuring can be substantial for the reactivity of the the material and its reducibility. The low-coordinated sites create defective states in the electronic structure and reduce the effective band gap, which can result in enhanced interaction with deposited species and modified photocatalytic activity.

[*] Corresponding author e-mail: gianfranco.pacchioni@mater.unimib.it

(tel. +39-2-6448-5219)

1. Introduction

Nanocrystalline structures have been of particular interest due to their novel fundamental properties and technological applications in numerous fields. The low-dimensionality of nanostructures causes quantum confinement effects that originate peculiar and size-dependent physical properties.[1] They exhibit chemical, optical, electronic and magnetic properties that are unique to the nanostructure regime,[2,3,4] and can be used as information storage media,[5,6] in biological labeling and detection,[7] catalysis[8,9] and photocatalysis,[10] among many other applications.

In the nanoscale regime, every single atom influences on the catalytic activity, and any mode of structural distortions may change such activity.[11] Nanocatalysis can then be viewed as a bridge between homogeneous and heterogeneous catalysis, where nanoparticles may combine the advantages of both fields offering unique activity and selectivity.[12] In other words, nanoparticles can be considered as discrete objects where the chemical processes take place at the interface with the environment. Thus, tailoring the catalytic activity of nanoparticles implies the understanding of their physical and chemical properties at the atomic scale.

Zirconium dioxide (ZrO_2) is an attractive material with broad technological applications. It is used in fuel cell electrolytes,[13] as gate dielectric[14] and chromatography support.[15] It has also been extensively used in catalysis, for example supporting Au, Ag and Cu catalysts in the water gas-shift reaction,[16] methanol synthesis from CO_2 and H_2,[17] CO oxidation,[18,19] and in the form of nanostructures, in photocatalytic reactions like CO_2 reduction.[20,21] However, the properties of zirconia depend on the different structural polymorphs. Zirconia shows three different stable phases. Up to 1175ºC the stables phase is the monoclinic one; at higher temperature it transforms into the tetragonal phase, stable up to 2370 ºC, and then into the cubic phase.[22,23] The cubic phase is a fluorite-type structure and the other two can be viewed as structural distortions from the cubic one. However, the room-temperature phase shows few practical applications.[24] Instead, the catalytic and mechanical interesting phase is the tetragonal (t-ZrO_2) one; for instance, it is used as superacid catalyst in hydrogenation and isomerization processes,[25] and as a superplastic ceramic.[26] To stabilize the tetragonal phase at lower temperatures, divalent and trivalent cationic species like Mg^{2+}, Ca^{2+} and Y^{3+} can be incorporated into the zirconia lattice.[27,28] On the other hand, to maintain the ZrO_2 purity, the tetragonal phase can be stabilized at room temperature in the form of nanostructures due to the differences in surface free energies in monoclinic

and tetragonal nanoparticles.[29] In fact, it has been found that it is possible to have tetragonal zirconia for nanoparticles smaller than 10 nm diameter,[30] or between 10 and 50 nm,[31] without doping.

Interesting features of metal oxides are intrinsic defects like oxygen vacancies, which are inevitably present after the synthesis involving high temperature processes and reducing atmospheres. A neutral O-vacancy introduces two extra electrons in the lattice, which can be either localized in the created vacancy or on cation sites nearby. In a non-reducible oxide like ZrO_2, the extra charge is trapped in the vacancy site rather than reducing the nearest Zr ions, generating defect states near the center of the electronic band gap. This picture is analogous to the F-centers found in MgO.[32,33] The presence of Zr^{3+} sites at the surface has been found experimentally, but in low amounts.[34] The F-center-like character of O-vacancies in zirconia has been theoretically predicted for the three phases,[35,36] and with formation energies in the range 5.6 – 5.9 eV[33,37-39] as predicted from first principles calculations in periodic systems. The role of nanostructuring and low-dimensionality on the stability of this point defect in zirconia has not been addressed yet and is one of the targets of this paper.

The theoretical investigation of bulk and nanostructured oxides is based on Density Functional Theory (DFT). DFT calculations can provide atomic-scale understanding of active sites in nanoparticles large enough to be scalable to bulk (100 or more atoms).[40-42] However, it is nowadays well established that the electronic band gap provided by the Kohn-Sham approach (KS gap) does not accurately reproduce the quasiparticle gap, which is measured by direct and inverse photoemission experiments.[33,43] The failure of the KS gap to reproduce the electronic gap is attributed to the known self-interaction error intrinsic in the Kohn-Sham implementation of DFT. To partly remove this error, the Hubbard correction[44] (DFT+U) and hybrid density functionals[45,46] have been considered through this work. The DFT+U methods penalize higher occupation of the band for which the U corrections is applied whereas hybrid functionals add a percentage of the exact Fock exchange to the semilocal exchange-correlation (*xc*) potential formulated within the Generalized Gradient Approximation (GGA). The fraction of the Fock exchange is connected to the dielectric constant of the material,[47] and the functional obtained with the optimum fraction of Fock exchange for bulk zirconia (20.8%) has provided quantitative agreement with experiments.[33,48] Note, however, that the dielectric constant of the ZrO_2 nanoparticles is unknown. Therefore, in this work, the standard PBE0 functional is instead used, which includes a fixed 25% of

Fock exchange.[46] This approach attenuates considerably the self-interaction error, yielding band gaps in better agreement with the experiment compared GGA functionals. [49] Nonetheless, the universal *xc* functional giving equally accurate description of all observables is still to be developed.

In this work, tetragonal zirconia nanoparticles up to 2 nm in size have been modeled. We provide a description of the thermodynamic stability and the electronic structure as a function of composition and particle size. On the methodological side, we also provide a comparison between properties calculated with different DFT approaches to treat the self-interaction error. Also, different basis sets (plane waves *versus* numerical) and treatments of core electrons (PAW *versus* all electron) are explored.

The paper is organized as follows. We first describe the computational approach in Section 2. Then, our models for zirconia nanoparticles are described in Section 3.1. The stability of the zirconia nanoparticles and the O-vacancies are addressed in Sections 3.2 and 3.3. We describe their electronic structure in Section 3.4. Finally, some general conclusions are summarized in Section 4.

2. Computational Details

Spin polarized DFT based calculations were performed using the Vienna Ab-initio Simulation Package (VASP 5.3),[50,51,52] where plane waves were used as basis with a kinetic energy cutoff of 400 eV. To describe the effect of the core electrons on the valence electron density, the projector augmented wave (PAW) method was used,[53,54] where O(2s, 2p) and Zr(4s, 5s, 4p, 4d) were considered as valence electrons and therefore treated explicitly. The Generalized Gradient Approximation (GGA) for the *xc* functional was applied within the Perdew, Burke and Ernzerhof (PBE) formulation.[55] To partly circumvent the self-interaction error of GGA functionals, also the PBE+U approach as proposed by Dudarev et al.[56,57] was used. The conduction band of zirconia is formed by the 4*d* states of Zr atoms (Figures S1-S3). Then, the multiple occupation of *d* orbitals is penalized so that the electron delocalization due to the self-interaction is attenuated. In particular, the onsite Coulomb correction (U_{eff} =U-J) for the Zr(4*d*) states was set to 4 eV. This value was found to provide a good description of the electronic as well as the geometric structure of bulk tetragonal zirconia.[37] The lattice parameters predicted by the PBE+U approach are a_0 = 3.662 Å and c_0 = 5.223 Å, in good agreement with the experimental parameters 3.64 and 5.27 Å, respectively.[58] Also, with our U_{eff} correction a band gap of 4.43 eV was obtained for bulk zirconia, still considerably

smaller than the experimental value 5.78 eV deduced from optical absorption measurements.[59]

Geometry optimization of the nanoparticles calculations were carried out at the *Γ*-point. All atoms were allowed to relax until the ionic forces are smaller than |0.01| eV/Å, with a total energy threshold determining the self-consistency of the electron density of 10^{-5} eV. On the other hand, calculations on bulk zirconia, to be taken as a reference, were performed with plane waves with kinetic energy up to 800 eV, and sampling the Brillouin zone in a 8×8×6 Monkhorst-Pack *k*-point grid. To obtain a reference of a periodic surface, *Γ*-point calculations with a cutoff of 400 eV were performed on a 3×2 slab of the (101) surface (180 atoms), with 20 Å of vacuum between the periodically repeated slabs.

The net charges of the ions were estimated from the Bader Atoms in Molecules topological analysis[60,61,62] The effective Bader charges are defined as $Q_{eff,i} = Z_{val,i} - q_i$, where $Z_{val,i}$ is the number of valence electrons of atom *i*, and q_i is the charge given by the Bader analysis.

For comparative purposes, DFT calculations were also performed using the FHI-AIMS 5.2 package,[63] where an all-electron atom-centered numerical basis set was employed. Also in this case the PBE exchange-correlation potential was considered,[55] and for a more accurate description of the electronic structure the full-range PBE0 hybrid functional was used, which includes a 25% of the Fock exchange.[46] Only the *Γ*-point was considered in calculations of the discrete nanoparticles; the threshold for the convergence of the electronic energy was set to 10^{-5} eV and all ions were relaxed up to ionic forces smaller than |0.01| eV/Å. The bulk and periodic surface references were also calculated on a 8×8× 6 and 1×1×1 *k*-point grids, respectively.

3. Results and discussion

3.1 Models of zirconia nanoparticles

To date, the determination of oxide nanostructures is far from being solved. This is partly due to the fact that experimental techniques aimed to elucidate the structure of such objects like neutron and X-ray diffraction do not provide a univocal picture.[64-66] Designing the structure of a representative model for zirconia nanoparticles is thus not an easy task. Numerous atomic configurations are possible, and even for small clusters, the potential energy surface is too complex to be explored with high-level ab-initio approaches. For applications in catalysis, our interest is more focused on relatively large

nanoparticles with properties that scale to the bulk regime[42,42] (but still computationally feasible). A good starting point is the design of nanoparticles based on the analysis of the lattice plane orientations in bulk zirconia. This is analogous to the Wulff construction at the nanoscale. Nevertheless, it has to be mentioned that whether the nanostructure is the global minimum or not is not an important issue in the investigation of catalytic reactions on surfaces.[67]

Thus, as starting geometries, bulk t-ZrO_2 was cleaved along the normal directions of the O-terminated {101} surfaces, resulting in nanoparticles with octahedral or bipyramidal shape. Then, the six corners of the octahedral structure were truncated giving a closed {101} object with O-terminated {001} facets at the corners (cuboctahedron). The design of octahedral and cuboctahedral morphologies for zirconia nanoparticles is consistent with the relative thermodynamic stability of the corresponding surfaces, being the O-terminated (101) and (001) surfaces the most stable ones in tetragonal zirconia.[68,69,70] An octahedron-based model has also been used for a Car-Parrinello Molecular Dynamics (MD) investigation of surface impurities on zirconia nanoparticles; this is also the stable shape when the nanoparticles are surrounded by water molecules.[71] Also, single-crystalline CeO_2 nanoparticles of 2 nm and more, with a fluorite-based structure like zirconia, are octahedral or cuboctahedral.[72] Neyman *et al.* found that the octahedral shape for ~1 nm ceria nanoparticles is the most stable one exploring the configurational space through a basin hopping algorithm.[73,74] It has also been found both experimentally[75,76] and by DFT calculations[77] that the chemically related TiO_2 material in the nanocrystalline regime adopts octahedral and truncated octahedral shapes in acidic conditions.

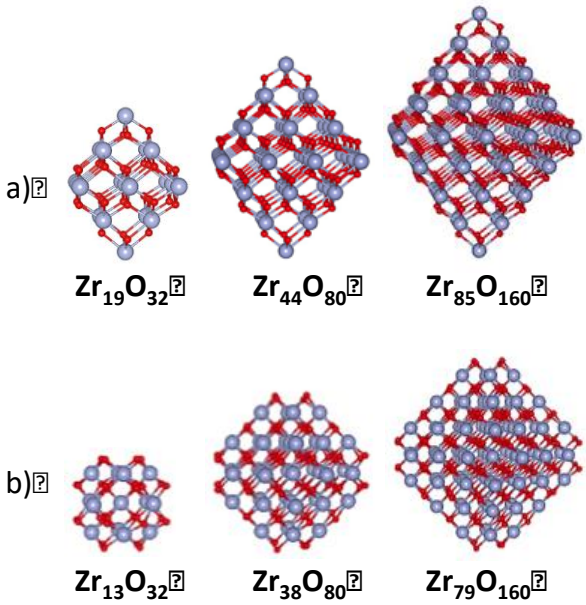

Figure 1. Models of (a) octahedral $(ZrO_{2-x})_n$, and (b) cuboctahedral zirconia nanoparticles $(ZrO_{2+x})_n$, created by removing the 6 Zr corner atoms from the octahedral configuration. Zr is represented by big blue atoms and O by red small atoms.

The octahedral models for zirconia nanoparticles are shown in Figure 1(a). The stoichiometries for this configuration are $Zr_{19}O_{32}$, $Zr_{44}O_{80}$ and $Zr_{85}O_{160}$, with optimized diameters 0.90, 1.40 and 1.92 nm (at PBE+U level of theory), respectively. These sizes are in the same range of synthesized octahedral-based zirconia nanoparticles (1.5 – 2.5 nm).[71] The cuboctahedral models, Figure 1(b), are obtained by removing the six low-coordinated Zr ions at the corners of the octahedron, giving respectively the nanoparticles $Zr_{13}O_{32}$, $Zr_{38}O_{80}$ and $Zr_{79}O_{160}$. In octahedrons and truncated octahedrons with O-terminated bulk-like {101} and {001} surfaces, the ZrO_2 stoichiometry cannot be maintained. To obtain the stoichiometric systems, instead of removing the excess O atoms from the cuboctahedral nanoparticles, which would lead to facets that do not display the same morphology as the bulk-like surfaces, a different number of Zr corner atoms must be removed. So, 3, 4 and 5 Zr corner atoms, respectively, were removed from the octahedrons resulting in $Zr_{16}O_{32}$, $Zr_{40}O_{80}$ and $Zr_{80}O_{160}$ nanoparticles, Figure 2. In this way the morphology of the bulk-like {101} and {001} terminations is maintained.

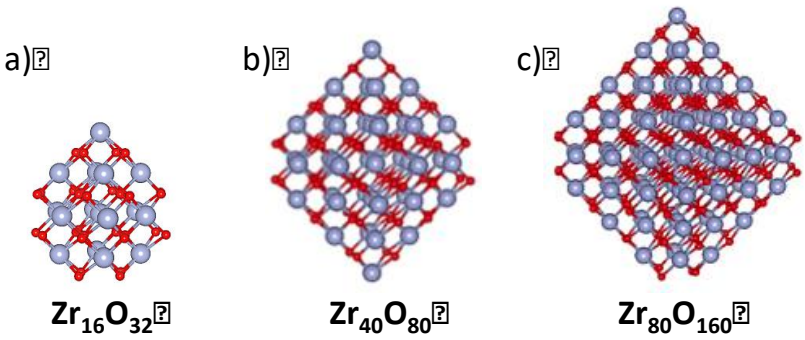

Figure 2. Models of partly truncated octahedral zirconia nanoparticles $(ZrO_2)_n$ created by removing (a) 3 Zr corner atoms from the $Zr_{19}O_{32}$ nanoparticle, (b) 4 Zr corner atoms from $Zr_{44}O_{80}$ and (c) 5 Zr corner atoms from $Zr_{85}O_{160}$. Zr is represented by big blue atoms and O by red small atoms.

After relaxation of the structure, the initial tetragonal phase is not maintained. This is more pronounced for the stoichiometric $Zr_{16}O_{32}$, $Zr_{40}O_{80}$ and $Zr_{80}O_{160}$ nanoparticles. Since these are octahedral objects only partly truncated, the structure is non-symmetric leading to larger distortions. In order to estimate the structural relaxation of the nanoparticles with respect to the bulk phase, the Zr-O and Zr-Zr bond distances calculated at PBE+U level are reported in Table 1. It is noteworthy that the PBE+U bond distances do not differ significantly from the PBE ones, giving bond lengths ~1.5% longer. In view of the variety of bond distances for each nanoparticle — due to different local relaxations caused by undercoordination — the minimum, maximum and average bond distances are reported. Both Zr-O and Zr-Zr bond distances are below those calculated in bulk t-ZrO_2. The ranges of variation are larger for the smallest nanoparticles due to higher local relaxations and loss of crystallinity. The longest Zr-Zr bond lengths are obtained for the cuboctahedral nanoparticles; these systems contain an excess of oxygen that makes Zr ions more positive, which increases the electrostatic repulsion between Zr ions.

Table 1. Optimized average coordination number of Zr ions, $\langle N \rangle_{Zr}$, and minimum, maximum and average Zr-O, $d_{Zr\text{-}O}$, and nearest Zr-Zr, $d_{Zr\text{-}Zr}$, bond distances (in Å). PBE+U results for partly truncated (PT) octahedral, octahedral and cuboctahedral nanoparticles compared with bulk t-ZrO_2.

	$\langle N \rangle_{Zr}$	$d_{Zr\text{-}O,\ min}$	$d_{Zr\text{-}O,\ max}$	$\langle d_{Zr\text{-}O} \rangle$	$d_{Zr\text{-}Zr,\ min}$	$d_{Zr\text{-}Zr,\ max}$	$\langle d_{Zr\text{-}Zr} \rangle$
ZrO_2 Bulk	8.00	2.16	2.30	2.23	3.66	3.68	3.67
PT Octahedral							
$Zr_{16}O_{32}$	5.38	1.94	2.49	2.14	2.97	3.65	3.35
$Zr_{40}O_{80}$	6.10	1.96	2.45	2.18	3.26	3.50	3.38
$Zr_{80}O_{160}$	6.75	2.04	2.92	2.20	3.37	3.54	3.44
Octahedral							
$Zr_{19}O_{32}$	5.47	2.11	2.24	2.18	3.18	3.18	3.18
$Zr_{44}O_{80}$	6.18	2.11	2.25	2.19	3.18	3.51	3.29
$Zr_{85}O_{160}$	6.59	2.09	2.40	2.22	3.28	3.67	3.54
Cuboctahedral							
$Zr_{13}O_{32}$	6.15	2.11	2.18	2.15	3.48	3.51	3.49
$Zr_{38}O_{80}$	6.42	2.03	2.44	2.18	3.29	3.57	3.43
$Zr_{79}O_{160}$	6.78	2.08	2.31	2.20	3.42	3.68	3.55

Although in these nanostructures the crystallinity of the tetragonal phase is not entirely conserved, the average Zr-Zr bond distance can provide an estimate of the degenerate lattice parameter a_0 of the tetragonal unit cell. The lattice parameters in the nanostructures are smaller than those calculated in bulk t-ZrO_2, a_0 = 3.66 Å and increase with the size of the nanoparticle as the bulk regime is approached. The size-dependence of the lattice constant is an expected behavior for nanoparticles, as a significant fraction of ions form shorter bonds to compensate the undercoordination (mainly surface ions). The lattice expansion with the size increase is also found in metal nanoparticles,[78] and its contraction with respect to the bulk is consistent with experimentally prepared 5 nm t-ZrO_2 nanoparticles by Yoshiasa *et al.*,[79] whose lattice parameter a_0 is measured to be 3.60 Å. Smaller (1.5 nm) nanoparticles prepared by Thomas *et al.*,[71] show nearest Zr-Zr bond distances of 3.5 Å, which are also below the bulk value.

It is worth noting that finding smaller lattice constants in the nanoparticles with respect to bulk is not a universal behavior. In the case of CeO_2, calculations predict

smaller lattice constants for nanoparticles than that for bulk ceria.[73,80] On the contrary, experimentally derived lattice constants are larger than the bulk one and they contract with particle size, which is also called *lattice anomaly*.[81,82] This has been attributed to the presence of reduced Ce^{3+} ions coming from O-vacancies that reduce the Ce-O electrostatic attraction.[73,81,82] In small clusters the fraction of Ce^{3+} ions is larger.[82] However, since differently from CeO_2, ZrO_2 is not reducible, a much lower number of oxygen vacancies are present and the *lattice anomaly* is not expected. In fact, in the prepared zirconia nanoparticles up to 5 nm less than 1% of Zr^{3+} centers were found.[79]

3.2 Formation energies of zirconia nanoparticles

The formation energies, E_f, are defined with respect to Zr bulk metal and molecular O_2 in the gas phase in its triplet ground state, according to

$$E_f = (1/n)\, E(Zr_nO_m) - E(Zr_{(s)}) - (m/2n)\, E(O_{2(g)}) \qquad (1)$$

In order to evaluate the effect of the different *xc* functionals, the formation energies have been computed at PBE, PBE+U and PBE0 levels of theory, Table 2. For comparison the formation energy of bulk t-ZrO_2 is also reported. All E_f values are given per Zr atom. PBE calculations have been performed with both plane wave and numerical basis sets. Both approaches give very similar PBE values, as expected. This allows us to use the PBE0 results for comparative purposes, despite the fact that these results are obtained only with a numerical basis set. In the rest of the work, we will refer to the PBE results calculated with plane wave basis set. Taking as a reference the PBE calculations, the Hubbard correction clearly leads to smaller formation energies (in absolute value) implying that fixing the gap has negative effects on the energetic stability. Instead, the PBE0 functional gives larger values although to a smaller extent. Moreover, the *U* correction is more size sensitive, being the formation energies 30% smaller than PBE ones in the smallest nanoparticles and 21% smaller in the bulk. Instead, the PBE0 results are always about 5% larger than the PBE ones, independent of the particle size. The PBE0 approach reproduces with greater accuracy the energetics of these systems giving the closest values to the experimental formation energy for bulk zirconia (-11.0 eV PBE0, -11.41 eV experiment).[83] Note, however, that the experimental value is obtained at 298.15 K and an accurate comparison with theoretical results would require extrapolation of the thermodynamic data to 0 K.

Table 2. Formation energies (in eV) per Zr atom from PBE, PBE+U and PBE0 calculations, for bulk t-ZrO_2, partly truncated (PT) octahedral, octahedral and cuboctahedral nanoparticles.

	PBE[a]	PBE[b]	PBE+U	PBE0
ZrO_2 Bulk	-10.30	-10.38	-8.19	-11.00
PT Octahedral				
$Zr_{16}O_{32}$	-8.61	-8.63	-6.27	-9.02
$Zr_{40}O_{80}$	-9.25	-9.30	-6.91	-9.73
$Zr_{80}O_{160}$	-9.48	-9.52	-7.17	-9.86
Octahedral				
$Zr_{19}O_{32}$	-7.43	-7.45	-5.03	-7.80
$Zr_{44}O_{80}$	-8.41	-8.44	-6.09	-8.88
Cuboctahedral				
$Zr_{13}O_{32}$	-7.74	-7.75	-5.33	-8.09
$Zr_{38}O_{80}$	-9.05	-9.07	-6.77	-9.59

[a]Computed with plane wave basis set.

[b]Computed with all-electron atom-centered numerical basis set.

We now consider the dependence of the formation energies on the average coordination number $<N>$ of Zr atoms (i.e. the average number of O ions directly coordinated to each Zr ion) from PBE+U results, Figure 3. The formation energies of the nanoparticles within the same configuration –octahedral, cubooctahedral and partly truncated octahedral – correlate linearly with $<N>$ and converge to the bulk value. To obtain a better linear correlation for octahedral and cubooctahedral nanoparticles, the formation energies of the $Zr_{85}O_{160}$ and $Zr_{79}O_{160}$ nanoparticles are also included (-6.65 and -7.18 eV with $<N>$ = 6.59 and 6.78, respectively). The partly-truncated octahedral nanoparticles exhibit the highest stability due to the fully stoichiometric composition. Nevertheless, it has to be taken into account that these nanoparticles have experienced a larger structural relaxation due to the non-symmetric cleavage of the corners, which may lower the energy (Section 3.1). The octahedral nanoparticles, despite they expose only the most stable (101) surface, are O-deficient and contain Zr ions in a reduced oxidation state with respect to that of bulk ZrO_2. This causes a destabilization due to the low reducible character of zirconia. These findings are in contrast to those obtained for

CeO_2 nanoparticles: ceria is a reducible oxide whose formation energies of O-deficient octahedral nanoparticles display the same stability and correlation as the stoichiometric ones.[73]

Despite the large amount of low-coordinated O ions (mainly in {001} facets), the cuboctahedral systems are only slightly destabilized with respect the stoichiometric structures. The destabilization is caused by the presence of peroxide-like O atoms from an O-rich stoichiometry. This is more pronounced for the smallest nanoparticle $Zr_{13}O_{32}$, which contains the highest O/Zr ratio and where all O ions of the surface are only 2-coordinated sites from the {001} facets. This nanoparticle has not been included in the linear fitting for cuboctahedral nanoparticles. From these findings, an important concept can be derived: from the correlation obtained, formation energies of nanoparticles with sizes not yet computationally feasible can be extrapolated.

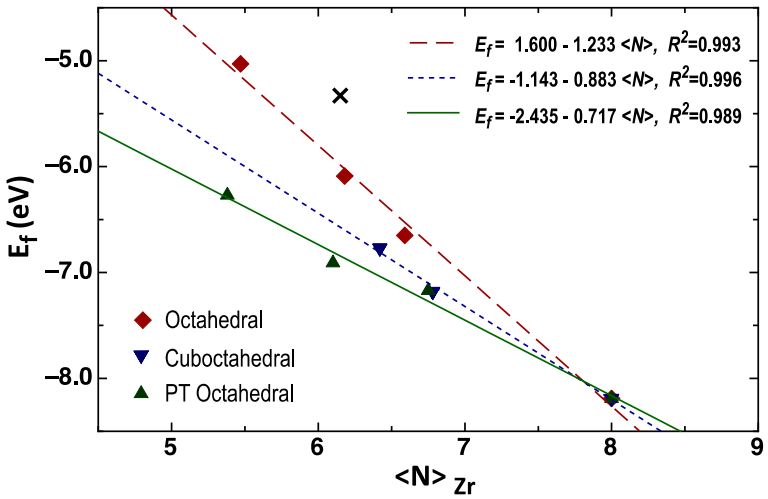

Figure 3. PBE+U formation energies (in eV) per Zr atom for octahedral, cuboctahedral, partly truncated (PT) octahedral zirconia nanoparticles and for bulk t-ZrO_2 (<N> = 8.0). The fitted correlation for each type of configuration is indicated. $Zr_{13}O_{32}$ is not included in the correlation for cuboctahedral nanoparticles (indicated with a cross).

3.3 Defective zirconia nanoparticles: oxygen vacancies

Oxygen vacancies are intrinsic defects of metal oxides with a great importance in catalysis.[84] The presence of O-vacancies in zirconia plays a fundamental role on its characteristic redox properties.[69] For instance, in chemical processes where O atoms are interchanged with molecules like CO, CO_2 or H_2O, either assisted by deposited metal

catalysts or directly acting as reactive centers. In this section, we investigate the stability of a neutral O-vacancy in the lattice of nanoparticles. We consider several sites with different coordination number of the O atoms that are removed. We define the formation energy (E_f) of the O-vacancies with respect to the formation of molecular oxygen,

$$E_f = E(Zr_nO_{m-1}) - E(Zr_nO_m) + \tfrac{1}{2}\, E(O_{2(g)}), \qquad (2)$$

where $E(Zr_nO_{m-1})$ and $E(Zr_nO_m)$ are the total energy of the nanoparticle with and without an O-vacancy, respectively, and $E(O_{2(g)})$ is the total energy of the O_2 molecule in its triplet ground state. The formation energies from PBE+U calculations are reported in Table 3. For comparison, those obtained for a periodic (101) zirconia surface are also reported.

We first consider the partly truncated or stoichiometric nanoparticles. For the extended (101) zirconia, the calculated formation energies of +5.97 (O_{3c}) and +5.67 eV (O_{4c}) surface are in very good agreement with previous results.[33,38,38] In the nanoparticles, as expected, the O_{2c} site (corner site) is the most favorable position for oxygen vacancy creation, with formation energies +3.94 ($Zr_{16}O_{32}$), +3.80 ($Zr_{40}O_{80}$) and +2.62 eV ($Zr_{80}O_{160}$). The energy required to create an O-vacancy decreases with the particle size. This trend agrees with the bond lengths that are found to increase with particle size (Section 3.1): longer distances imply weaker bonds that reduce the cost to create a vacancy.

In general, the stability of these defects depends mainly on two aspects: the localization of the excess electrons after the O removal (electronic effect) and the relaxation of the lattice around the vacancy (geometric effect). In order to analyze the structural effect, we also computed the O vacancy formation energies of stoichiometric nanoparticles but without allowing the ions to relax in response to the creation of the vacancy. The large energy difference between these calculations implies that the structural rearrangement around the vacancy plays an important role. This is found in the few cases where the preferred electronic state of the excess charge is the triplet state, that is, the two extra electrons reduce two Zr ions near the vacancy. In these cases, the relaxation energies are between 1.7 – 2.1 eV. Instead, the relaxation is less pronounced when the electrons are mainly localized in the vacancy forming a non-magnetic state. This is the common situation in F-centers in ionic crystals like MgO.[32] In these cases, the relaxation energies are between 0 – 1.5 eV. However, the inner O_{4c}-vacancy in the $Zr_{80}O_{160}$ nanoparticle undergoes a significant structural relaxation that lowers

considerably the energy, despite the F-center-like behavior. This is an internal vacancy that should play a minor role in O-mediated surface reactions.

Hence, several factors determine the stability of the O-vacancies. These factors become even more important when the material is nanostructured. A clear general trend to predict the stability, preferred positions and electronic ground state of O-vacancies at the nanoscale cannot be easily defined as in bulk zirconia. Nevertheless, there are no important changes in the stabilities of O_{3c}- and O_{4c}-vacancies when the extended surface and nanoparticles are compared (even including corner-O_{3c} sites). The formation energy is reduced up to 1 eV in $Zr_{16}O_{32}$ and $Zr_{40}O_{80}$, although $Zr_{80}O_{160}$ is an exception due to an important contribution of the structural relaxation of the inner O_{4c}-vacancy. However, O atoms in low-coordinated sites are easy to remove (corner-O_{2c} and O_{3c}), representing the important catalytic sites in redox reactions where the transfer of an O atom is implied. In addition, the tendency to trap the excess electrons in the vacancy sites rather than to reduce Zr ions is found also in zirconia nanoparticles. The energy differences between the closed-shell singlet and triplet states are quite small, being in most cases between 0.01 and 0.20 eV; the electron localization becomes less relevant under real conditions where the (high) temperature may overcome this energy difference.

Since the octahedral nanoparticles are already reduced systems, the stability of the O-vacancies follows a different trend compared to the stoichiometric ones. These nanoparticles already contain electron density localized on surface Zr sites and interstitial positions, as it will be further discussed in the next section. In these systems, the excess electrons introduced after the creation of an O-vacancy are less stable, resulting in higher formation energies than for stoichiometric nanoparticles. In particular, without relaxation, the formation energy of the O-vacancy at the surface increases to +6.50 and +6.10 eV in $Zr_{19}O_{32}$ and $Zr_{44}O_{80}$, respectively. Then, in these cases, the vacancies are mainly stabilized by relaxation effects, lowering E_f to +6.11 and +5.86 eV in $Zr_{19}O_{32}$ and $Zr_{44}O_{80}$, respectively, Table 3. This also reflects in the smallest formation energies of inner-O_{4c}, where the ionic relaxation turns out to be more important.

Table 3. Formation energies (in eV) of *n*-coordinated O_{nc}-vacancies of partly truncated (PT) octahedral, octahedral and cuboctahedral zirconia nanoparticles, in singlet (S) or triplet (T) electronic configuration. For comparison, an O_{nc}-vacancy in the (101) surface (3×2 slab, corresponding to a 1/12 coverage of O-vacancies) of t-ZrO_2 are also reported.

System	Corner – O_{2c}	Corner – O_{3c}	Facet – O_{3c}	Inner – O_{4c}
t-ZrO_2 (101)	-	-	+5.97 (S)	+5.67 (S)
PT Octahedral				
$Zr_{16}O_{32}$	+3.94 (S)	-	+5.89 (S)	+5.15 (S)
$Zr_{40}O_{80}$	+3.70 (S)	+4.16 (T)	+4.86 (T)	+5.11 (S)
$Zr_{80}O_{160}$	+2.62 (S)	+5.26 (S)	+4.42 (T)	+2.17 (S)
Octahedral				
$Zr_{19}O_{32}$	-	+6.11 (S)	-	+4.16 (S)
$Zr_{44}O_{80}$	-	+5.86 (T)	+5.69 (S)	+4.74 (S)
Cuboctahedral				
$Zr_{13}O_{32}$	-2.35	-	-	-2.63
$Zr_{38}O_{80}$	-1.02	-	-1.02	-0.10

Clearly, cuboctahedral nanoparticles represent a special case. These are oxidized systems, with an O-rich stoichiometry. Then, the removal of an O atom from the lattice is an exothermic process; in other words, cuboctahedral nanoparticles are thermodynamically unstable with respect the spontaneous formation of $O_{2(g)}$. This is more evident in $Zr_{13}O_{32}$, which already showed a low stability with respect the decomposition into bulk $Zr_{(s)}$ and molecular $O_{2(g)}$ in comparison with the other systems (Section 3.2). The instability of these systems is attributed to the models selected for this morphology. The cuboctahedral nanoparticles have been constructed exhibiting bulk-like O-terminated (101) surfaces. However, previous DFT calculations predicted that 1 – 1.5 nm oxide nanoparticles do not exhibit the bulk-like surface morphology in oxidizing environments.[85] Rather, the oxidized nanoparticles are passivized with molecular O_n^m groups adsorbed on the surface, with peroxide-like O atoms. These trends follow from a study referring to ceria nanoparticles, but this is likely to occur

also in oxidized ZrO_{2+x} nanoparticles.[71] Sufficiently large nanoparticles, instead, contain enough O-vacancies in the bulk to compensate the O-rich surfaces and stabilize the bulk-like O-terminated morphology.

3.4. Electronic structure of zirconia nanoparticles

Detailed information on the electronic structure of zirconia nanoparticles is obtained from the Projected Density of States (PDOS). Moreover, the performance of the different methodologies in determining the Kohn-Sham (KS) band gap and possible defect states is also tested by the calculation of the PDOS. The PDOS plots computed with PBE, PBE+U and PBE0 functionals for stoichiometric zirconia nanoparticles are shown in Figure 4. There are no significant qualitative variations between the PBE PDOS plots computed with plane wave and numerical basis sets, so only the latter are not shown for simplicity.

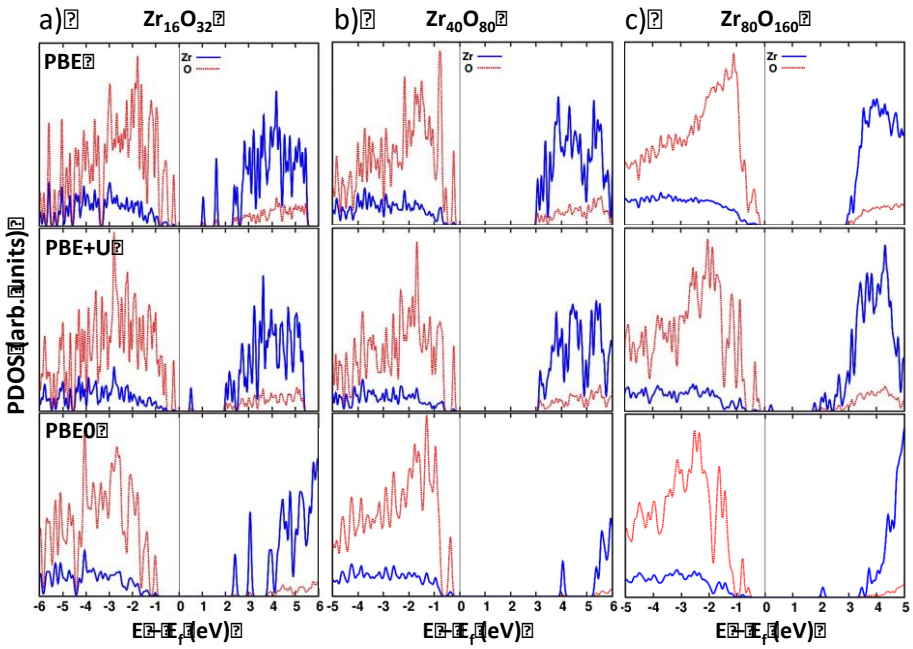

Figure 4. Projected Density of States of a) $Zr_{16}O_{32}$, b) $Zr_{40}O_{80}$ and c) $Zr_{80}O_{160}$ nanoparticles, from (top to bottom) PBE, PBE+U and PBE0 calculations. The zero of energy corresponds to the Fermi level.

Nanoparticles with a stoichiometric composition are partly truncated octahedrons that contain both low-coordinated Zr and O ions (Section 3.1). These sites give rise to defective states in the electronic structure that are separated from the valence (O sites) and conduction (Zr sites) bands, narrowing therefore the band gap. This is more

pronounced in the smallest nanoparticle $Zr_{16}O_{32}$ which displays the highest ratio of undercoordinated sites, Figure 4(a). In this case, the presence of defect states does not allow us to determine the band gap, since the edges of the valence (VB) and conduction bands (CB) cannot be easily identified, pointing to the molecular nature of this system.

Not surprisingly, the different level of theory clearly plays a role in defining the electronic structures of these systems. The KS band gaps of stoichiometric nanoparticles predicted by the different approaches are reported in Table 4, together with those of bulk zirconia and of the (101) surface and some experimental findings. In the nanoparticles, we have considered the energy gap between the highest occupied and lowest unoccupied electronic states, but we did not consider the defective states due to low-coordinated sites. Note that the distinction between a defect state and states belonging to the VB or CB is not always easy. In particular, to define a state as defect state we have examined whether the electron densities projected on the KS eigenvalues around the Fermi level are localized on low-coordinated sites (*i.e.* a corner Zr ion or at the O_{2c} ions of a {001} facet). As expected, the KS band gaps obtained at PBE level are underestimated, due to the self-interaction error inherent in GGA *xc* functionals. The Hubbard correction on the PBE functional enhances the band gap which however remains below the experimental value, while the hybrid PBE0 functional seems to slightly overestimate the gap with respect to the experiment. The same trend has been found in both nanostructures and periodic systems (bulk or surface). The interesting feature of the electronic structure of these nanoparticles is the presence of defect gap states from low-coordinated sites of stoichiometric particles, an effect that effectively reduces the transition energies. This may have the consequence to enhance the interaction of the nanoparticles with metal catalysts as well as their photocatalytic activity.

The overestimation of the KS gap at the PBE0 level of theory was also found in previous theoretical studies on bulk tetragonal zirconia.[86] However, it is important to mention that the experimental values cannot be solely attributed to the tetragonal phase since they were obtained from measurements on amorphous or polycrystalline samples. The definition of the band gap with the various experimental techniques may differ from the KS band gap provided by the DFT calculations. We compare the results with band gap values from photoemission experiments (PES+IPS, 5.5[87] and 5.68[88] eV), which probe the energy difference between the N and N±1 electron system — fundamental band gap — as well as from optical measurements (VUV, 5.78[59] eV),

which involve excitations providing the optical gap. This value, however, differs from the electronic band gap in the exciton binding energy. Also, our calculations do not consider electron-phonon interactions. These are known to reduce the band gap with respect to the 0 K fundamental gap[89,90] so they may be another source of possible disagreement between theory and experiment.

Table 4. Band gaps (eV) of bulk, (101) surface and stoichiometric nanoparticles of t-ZrO_2 from PBE, PBE+U and PBE0 calculations.

	PBE[a]	PBE[b]	PBE+U	PBE0
Bulk ZrO_2	3.72	3.75	4.43	6.13
t-ZrO_2 (101)	3.45	3.56	4.01	5.94
$Zr_{16}O_{32}$ [c]	1.27	1.35	0.75	3.44
$Zr_{16}O_{32}$ [d]	3.26	3.32	3.28	5.33
$Zr_{40}O_{80}$ [c]	3.27	3.22	3.37	4.40
$Zr_{40}O_{80}$ [d]	3.59	3.22	3.80	6.12
$Zr_{80}O_{160}$ [c]	3.22	3.20	0.44	2.67
$Zr_{80}O_{160}$ [d]	3.61	3.41	3.63	5.20
Experiment				
Bulk ZrO_2	5.5[e] 5.68[f] 5.78[g]			

[a]Computed with plane wave basis set.

[b]Computed with all-electron atom-centered numerical basis set.

[c]Difference between the highest occupied and the lowest empty states.

[d]Difference between the estimated edges of valence and conduction bands.

[e]Photoemission Spectroscopy + Inverse Photoemission Spectroscopy (PES+IPS), Ref. 87

[f]Photoemission Spectroscopy + Inverse Photoemission Spectroscopy (PES+IPS), Ref. 88

[g]Reflectance Spectroscopy (VUV) in Y-doped ZrO_2, Ref. 59

In general, the role of the different computational approaches used is the same for periodic zirconia and nanoparticles. Defining the best DFT approach may depend on the observable of interest. For instance, the PBE0 hybrid functional overestimates the KS band gap but it reproduces quite accurately the energetics of the zirconia nanoparticles (Section 3.2). On the other hand, the Hubbard correction is a less expensive computational approach that partly corrects the KS band gap but significantly underestimates the formation energies. Then, the PBE0 functional would be a suitable choice to model the zirconia nanoparticles. However, any of the different approaches

here considered provides the correct trend between the band gap and the size of the nanoparticles.

Octahedral zirconia nanoparticles display a different electronic structure. These nanoparticles are oxygen deficient; that is, there is an excess of electrons not compensated by O atoms, so that the electronic structure is equivalent to that of reduced zirconia with O vacancies that induce defect states in the gap (mainly Zr 4*d* states, Figure S2). The $Zr_{19}O_{32}$ stoichiometry is equivalent to six O-vacancies in a regular lattice; the $Zr_{44}O_{80}$ nanoparticle to eight O-vacancies, and $Zr_{85}O_{160}$ to ten O-vacancies, meaning that there are 12, 16 and 20 extra valence electrons, respectively. These electrons can arrange in a high or in a low-spin state, like the electrons from an O-vacancy which can form a triplet or a singlet state, respectively (Section 3.3).[35-39] The electronic ground state of the zirconia nanoparticles is non-magnetic. This is in contrast with ceria octahedral nanoparticles where the ground state is high-spin, due to the high spin coupling of the Ce^{3+} ions.[73] By plotting the electron density projected on the KS energies belonging to the defective Zr gap states (Figure 5 for $Zr_{44}O_{80}$), we confirm that the extra electrons are mainly localized on the six Zr corner ions. This implies the lowest number of Zr ions with a reduced effective charge, in contrast to the 12 ($Zr_{19}O_{32}$), 16 ($Zr_{44}O_{80}$) and 20 ($Zr_{85}O_{160}$) Zr ions that are reduced in the high-spin state. Thus, the singlet ground state is favored.

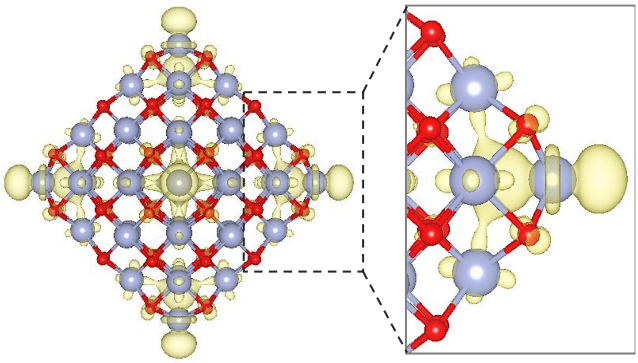

Figure 5. Electron density plot (PBE+U) projected on the KS energies corresponding to Zr gap states for the $Zr_{44}O_{80}$ nanoparticle. Zr is represented by big blue atoms and O by red small atoms. ρ_{iso}=0.007 e/Å^3.

The computed net charges on the six Zr corner ions are smaller in the singlet ground state than in the high-spin state (+1.70 - 1.72|e| *versus* +1.94 - 2.20|e|, being

+2.60 - 2.70|e| on inner Zr ions). On the other hand, the d_{z^2} shape of the density can be identified around the Zr corners with higher localization in the interstitial site, Figure 5. This means that the excess electron density is shifted towards the interstice rather than localized on the Zr ion. This is consistent with the preference of O-deficient zirconia to create singlet F-centers localized in the vacancy site rather than reducing two Zr ions.

The energy difference between low and high-spin states, ΔE, depends on the functional used. In particular, the PBE+U and PBE0 approaches stabilize the high-spin state with respect to PBE. For $Zr_{19}O_{32}$, ΔE = +3.82 eV at PBE level but ΔE = +2.10 and +2.48 eV at PBE+U and PBE0 levels, respectively; for $Zr_{44}O_{80}$, ΔE = +3.81 eV at PBE level and ΔE = +1.69 and +1.99 eV at PBE+U and PBE0 levels, respectively. This can be explained by the higher electron localization on Zr in the high-spin state that is more pronounced in DFT+U and hybrid functionals.

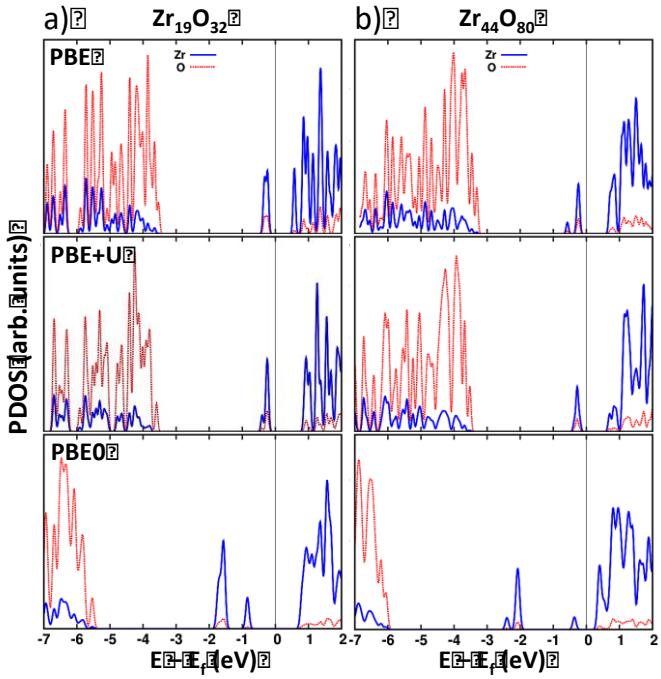

Figure 6. Projected Density of States of a) $Zr_{19}O_{32}$ and b) $Zr_{44}O_{80}$ nanoparticles in the electronic ground state (low-spin state), obtained (top to bottom) at PBE, PBE+U and PBE0 levels. The zero of energy corresponds to the Fermi level.

The ground state PDOS for the octahedral $Zr_{19}O_{32}$ and $Zr_{44}O_{80}$ nanoparticles are shown in Figure 6. As found with the stoichiometric nanoparticles, the VB-CB energy gap is increased with PBE+U and PBE0 functionals. However, the relative position of the defect states due to the O deficiency is not significantly affected by the U correction.

In $Zr_{19}O_{32}$, such Zr gap states appear 3.2 eV above the VB, and 0.8 and 1.1 eV below the CB in the PBE and PBE+U calculations, respectively, Figure 6(a). In $Zr_{44}O_{80}$, they appear 0.9 eV below the CB, and 3 and 3.1 eV above the VB in PBE and PBE+U, Figure 6(b). Upon application of the Hubbard U correction the overall increase of the band gap is of 0.1 – 0.3 eV. The hybrid PBE0 functional has a more pronounced effect: the KS band gaps are of 6.3 eV in $Zr_{19}O_{32}$ and 6.1 eV in $Zr_{44}O_{80}$, and the gap states are 3.8 and 3.7 eV above the VB, respectively, Figure 6(a,b). The high-spin excited state, in contrast, shows splitting of the defect states in the band gap, due to higher localization of the electron density in different Zr sites -corners and edges- that display different stabilities, Figure 7.

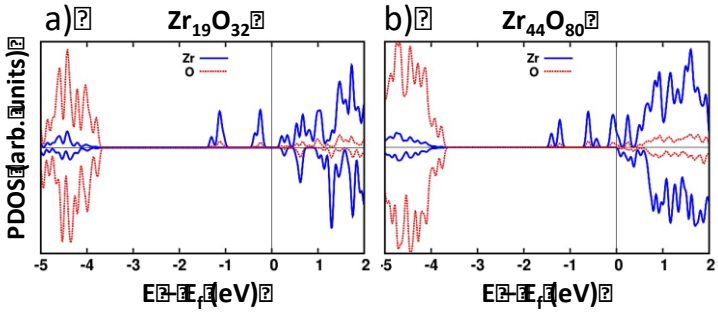

Figure 7. Projected Density of States of (a) $Zr_{19}O_{32}$ and (b) $Zr_{44}O_{80}$ nanoparticles in the high-spin excited state, from PBE+U calculation. The zero of energy corresponds to the Fermi level.

It is important to note that these nanoparticles display electronic structures analogous to that of bulk/surface zirconia with O-vacancies, with high-lying donor states in band gap. Hence, the interaction with a metal catalyst can be dominated by electronic effects which involve charge transfer from the donor states of the nanoparticle and the metal, without the inducing the pronounced structural relaxation and rearrangement typical in supports with a vacancy in the lattice.

Finally, cuboctahedral zirconia nanoparticles are characterized by an O-rich composition, which yields peculiar electronic and magnetic properties. As it has been explained above, the cuboctahedral nanoparticles considered in this work exhibit bulk-like O-terminated surfaces. Formally, there are six excess O atoms in $Zr_{13}O_{32}$, four in $Zr_{38}O_{80}$ and two in $Zr_{79}O_{160}$. Of course, these atoms are not fully reduced and maintain an atom-like electronic configuration with two unpaired electrons in O_{2p} levels (Figure

S3). This results in a global net magnetic moment of twelve, eight, and four unpaired electrons in the ground state of $Zr_{13}O_{32}$, $Zr_{38}O_{80}$ and $Zr_{79}O_{160}$, respectively, with the spin density localized on the surface O ions.

The PDOS plots for $Zr_{13}O_{32}$ and $Zr_{38}O_{80}$ nanoparticles are shown in Figure 8, for PBE, PBE+U and PBE0 calculations. The partial occupation of the O_{2p} states introduces low-lying empty states in the band gap that may behave as acceptor states in interaction with metal particles or other donor species. The PBE+U approach shifts the conduction band upwards but the O_{2p} empty gap states are unchanged in $Zr_{38}O_{80}$ (1.0-1.1 eV above the VB), while they are slightly shifted downwards in $Zr_{13}O_{32}$ (from 0.9-1.1 eV above the VB at PBE level, around 0.5 eV above the VB in PBE+U). This is attributed to the fact that the Hubbard correction is applied only to Zr(*d*) states, which are the main contributors to the conduction band. Instead, the PBE0 density functional introduces the fraction of Fock exchange in the functional on all electronic state on an equal footing.

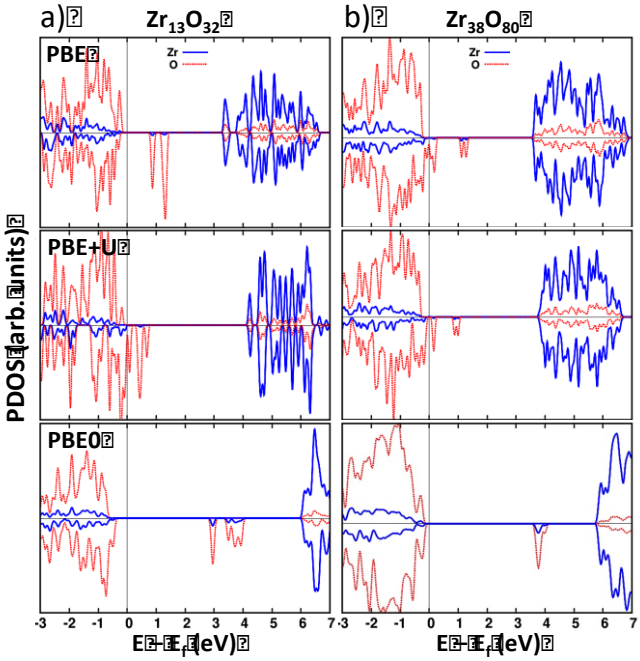

Figure 8. Projected Density of States of a) $Zr_{13}O_{32}$ and b) $Zr_{38}O_{80}$ nanoparticles in the electronic ground state, from (top to bottom) PBE, PBE+U and PBE0 calculations. The zero of energy corresponds to the Fermi level.

The calculated Bader charges on the Zr ions do not differ significantly from those in bulk zirconia: +2.69, +2.70 and +2.73 |e| in $Zr_{13}O_{32}$, $Zr_{38}O_{80}$ and $Zr_{79}O_{160}$, respectively, being +2.77 |e| the value in bulk zirconia. This indicates that the Zr ions

are not oxidized beyond the bulk oxidation state. Instead, the surface O ions show lower charges (in absolute value) than those in the bulk, which correspond to peroxide-like oxygens: -1.01, -1.15 and -1.19 |e| in $Zr_{13}O_{32}$, $Zr_{38}O_{80}$ and $Zr_{79}O_{160}$, respectively, while the corresponding value in bulk zirconia is -1.39|e|.

Hence, these nanoparticles have a strong oxidizing power due to the presence of acceptor gap states or to the presence of peroxide-like O ions forming O_n^m groups adsorbed on the surface that can react with adsorbed species (Section 3.3). However, we mentioned already that this situation is not thermodynamically favorable, and the preference is to desorb O_2 molecules (Section 3.3).

4. Conclusions

In this work, we have designed a set of different models for zirconia nanoparticles with sizes in the 0.9 – 1.9 nm range. These nanoparticles are built based on the relative stability of the exposed facets and taking different stoichiometries into account. Their properties have been compared with PBE, PBE+U and PBE0 density functionals.

Nanoparticles exposing {101} and {001} facets with stoichiometric composition are the most stable ones. Instead, those exhibiting only the most stable surfaces {101} show the lowest stability due to the presence of several reduced Zr ions. Therefore, the relative stability of the exposed facets, which is the main argument behind Wulff constructions, is not large enough to predict the stability of a given morphology, but also the electronic structure of the current stoichiometry plays an important role. Importantly, the calculated formation energies correlate linearly with the particle size and converge to the bulk value. Moreover, the stabilization of O-vacancies in the nanostructure regime is strongly influenced by structural and electronic effects (*i.e.* ionic relaxation and electron localization), which makes it difficult to provide a clear trend for the O-vacancy formation energies.

Low-coordinated sites in stoichiometric nanoparticles introduce defective states in the band gap separated from the VB and CB, reducing the effective band gap. These are reactive sites that enhance the interaction with deposited metal catalysts, as well as the photocatalytic activity by modification of the transition energies. As expected, reduced and oxidized nanoparticles show Zr(*d*) donors and O(*p*) acceptors states in the band gap, respectively.

Regarding the methodology, PBE+U and PBE0 approaches improve considerably the electronic structure with respect to the PBE functional. However, the PBE+U

method underestimates the formation energies, which are below those obtained at the PBE level. PBE0, instead, provides the closest formation energies to the experiment. The same trends are obtained in both nanostructure and bulk regimes. Thus, a compromise is required between computational cost (hybrid functionals) and the accurate description of each observable in the application of the proper method on metal oxide nanostructures.

In the bulk regime, zirconia is an insulator with low chemical activity. In the nanostructure regime it shows special electronic properties tunable with size and shape that make zirconia nanoparticles of special interest in catalysis.

Aknowledgement. We thank Dr. S. Tosoni for useful discussions. The work has been supported by the European Union's Seventh Framework Programme FP7/2007-2013 under (a) Grant Agreement nº 607417 - European Marie Curie Network CATSENSE, and (b) Grant Agreement n° 604307 - CASCATBEL, and by Italian MIUR through the FIRB Project RBAP115AYN "Oxides at the nanoscale: multifunctionality and applications". The research carried out at the *Universitat de Barcelona* was supported by the Spanish MINECO grant CTQ2012-30751 and, in part, by *Generalitat de Catalunya* (grants 2014SGR97 and XRQTC). Computational time at the *MARENOSTRUM* supercomputer has been provided by the Barcelona Supercomputing Centre (BSC) through a grant from *Red Española de Supercomputación* (RES). The support of the COST Action CM1104 "Reducible oxide chemistry, structure and functions" is also acknowledged.

Supporting Information Available: Density of States (DOS) for zirconia nanoparticles in the electronic ground state projected on *s*, *p* and *d* orbitals; and cartesian coordinates (Å) of the optimized zirconia nanoparticles as predicted from calculations using plane waves and numerical basis sets. This information is available free of charge via the Internet at http://pubs.acs.org.

References

[1] Dosch, H. Some General Aspects of Confinement in Nanomaterials. *Appl. Surf. Sci.,* **2001**, *182, 471-495.*

[2] Alivisatos, A. P. Semiconductor clusters, nanocrystals, and quantum dots. *Science,* **1996**, *271, 933-937.*

[3] Hyeon, T. Chemical Synthesis of Magnetic Nanoparticles. *Chem. Commun.,* **2003**, *927-934.*

[4] Majetich, S. A.; Jin, Y. Magnetization Directions of Individual Nanoparticles. *Science,* **1999**, *284, 470-473.*

[5] Black, C. T.; Murray, C. B.; Sandstrom, R. L.; Sun, S. Spin-dependent Tunneling in Self-Assembled Cobalt-Nanocrystal Superlattices. *Science,* **2000**, *290, 1131-1134.*

[6] Sun, S.; Murray, C. B.; Weller, D.; Folks, L.; Moser, A. Monodisperse FePt Nanoparticles and Ferromagnetic FePt Nanocrystal Superlattices. *Science,* **2000**, *287, 1989-1992.*

[7] Bruchez, M.; Moronne, M.; Gin, P.; Weiss, S.; Alivisatos, A. P. Semiconductor Nanocrystals as Fluorescent Biological Labels. *Science,* **1998**, *281, 2013-2016.*

[8] Kim, S.W.; Kim, M.; Lee, W. Y.; Hyeon, T. Fabrication of Hollow Palladium Spheres and Their Successful Application to the Recyclable Heterogeneous Catalyst for Suzuki Coupling Reactions. *J. Am. Chem. Soc.,* **2002**, *124, 7642-7643.*

[9] Kim, S. W.; Son, S. U.; Lee, S. S.; Hyeon, T.; Chung, Y. K. Colloidal Cobalt Nanoparticles: A Highly Active and Reusable Pauson–Khand catalyst. *Chem. Commun.,* **2001**, *2212-2213.*

[10] Hagfeldt, A.; Grätzel, M. Light-Induced Redox Reactions in Nanocrystalline Systems. *Chem. Rev.* **1995**, *95, 49-68.*

[11] Gilbert, B.; Huang, F.; Zhang, H.; Wayhunas, G. A.; Banfield, J. F. Nanoparticles: Strained and Stiff. *Science,* **2004**, *305, 651-654.*

[12] Somorjai, G. A.; Contreras, A. M.; Montano, M.; Rioux, R. M. Clusters, Surfaces and Catalysis. *Proc. Natl. Acad. Sci. USA,* **2006**, *103, 10577-10583.*

[13] Badwal, S. P. S. Yttria Tetragonal Zirconia Polycrystalline Electrolytes for Solid State Electrochemical Cells. *Appl. Phys. A,* **1990**, *50, 449-463.*

[14] Wilk, G. D.; Wallace, R. M.; Anthony, J. M. High-κ Gate Dielectrics: Current Status and Materials Properties Considerations. *J. Appl. Phys.,* **2001**, *89, 5243-5275*.

[15] Nawrocki, J.; Dunlap, C.; Li, J.; Zhao, J.; McNeff, C. V.; McCormik, A.; Carr, P. W. Chromatography Using Ultra-Stable Metal Oxide-Based Stationary Phases for HPLC. *J. Chromatogr. A,* **2004**, *1028, 31-62.*

[16] Idakiev, V.; Tabakova, T.; Naydenov, A.; Yuan, Z. Y.; Su, B. L. Gold Catalysts Supported on Mesoporous Zirconia for Low-Temperature Water–Gas Shift Reaction. *Appl. Catal. B,* **2006**, *63, 178-186.*

[17] Koeppel, R. A.; Baiker, A.; Schild, C.; Wokaun, A. Carbon Dioxide Hydrogenation over Au/ZrO_2 Catalysts from Amorphous Precursors: Catalytic Reaction Mechanism. *J. Chem. Soc., Faraday Trans.,* **1991**, *87, 2821-2828.*

[18] Zhang, X.; Wang, H.; Xu, B. Q. Remarkable Nanosize Effect of Zirconia in Au/ZrO_2 Catalyst for CO Oxidation. *J. Phys. Chem. B,* **2005**, *109, 9678-9683.*

[19] Comotti, M.; Li, W. C.; Spliethoff, B.; Schuth, F. Support Effect in High Activity Gold Catalysts for CO Oxidation. *J. Am. Chem. Soc.,* **2006**, *128, 917-924.*

[20] Sayama, K.; Arakawa, H. Photocatalytic Decomposition of Water and Photocatalytic Reduction of Carbon Dioxide over Zirconia Catalyst *J. Phys. Chem.,* **1993**, *97, 531-533.*

[21] Kohno, Y.; Tanaka, T.; Funabiki, T.; Yoshida, S. Photoreduction of Carbon Dioxide with Hydrogen over ZrO_2. *Chem. Commun.* **1997**, *841-842.*

[22] Dwivedi, A.; Cormack, A. N. A Computer Simulation Study of the Defect Structure of Calcia-Stabilized Zirconia. *Philos. Mag.* **1990**, *61, 1-22.*

[23] Kharton, V. V.; Marques, F. M. B.; Atkinson, A. Transport Properties of Solid Oxide Electrolyte Ceramics: A Brief Review. *Solid State Ionics,* **2004**, *174, 135-149.*

[24] Shukla, S.; Seal, S. Mechanisms of Room Temperature Metastable Tetragonal Phase Stabilisation in Zirconia. *Int. Mater. Rev.,* **2005**, *50, 45-64.*

[25] Hino, M; Arata, K. Synthesis of Solid Superacid Catalyst with Acid Strength of $H_0 \leq -16.04$. *J. Chem. Soc. Chem. Commun.,* **1980**, *851-852.*

[26] Chen, I. W.; Xue, L. A. Development of Superplastic Structural Ceramics. *J. Am. Ceram. Soc.,* **1990**, *73, 2585-2609.*

[27] Štefanić, G.; Musić, S. Factors Influencing the Stability of Low Temperature Tetragonal ZrO_2. *Croat. Chem. Acta,* **2002**, *75, 727-767.*

[28] Garvie, R. C.; Hanink, R. H. J.; Pascoe, R. J. Ceramic steel? *Nature*, **1975**, *258, 703-704.*

[29] Garvie, R. C. The Occurrence of Metastable Tetragonal Zirconia as a Crystallite Size Effect. *J. Phys. Chem.,* **1965**, *69, 1238-1243.*

[30] Garvie, R. C. Stabilization of the Tetragonal Structure in Zirconia Microcrystals. *J. Phys. Chem.*, **1978**, *82, 218-224.*

[31] Shukla, S.; Seal, S. Thermodynamic Tetragonal Phase Stability in Sol-Gel Derived Nanodomains of Pure Zirconia. *J. Phys. Chem. B,* **2004**, *108, 3395-3399.*

[32] Kantorovich, L. N.; Holender, J. M.; Gillan, M. J. The Energetics and Electronic Structure of Defective and Irregular Surfaces on MgO. *Surf. Sci.,* **1995**, *343, 221-239.*

[33] Gerosa, M.; Bottani, C. E.; Caramella, L.; Onida, G.; Di Valentin, C.; Pacchioni, G. Defect Calculations in Semiconductors Through a Dielectric-Dependent Hybrid DFT Functional: The Case of Oxygen Vacancies in Metal Oxides. *J. Chem. Phys.*, **2015**, *143, 134702-134710.*

[34] Morterra, C.; Giamello, E.; Orio, L.; Volante, M. Formation and Reactivity of Zirconium (3+) Centers at the Surface of Vacuum-Activated Monoclinic Zirconia. *J. Phys. Chem.*, **1990**, *94, 3111-3116.*

[35] Eichler, A. Tetragonal Y-Doped Zirconia: Structure and Ion Conductivity. *Phys. Rev. B,* **2001**, *64, 174103-174111.*

[36] Králik, B.; Chang, E. K.; Louie, S. G. Structural Properties and Quasiparticle Band Structure of Zirconia. *Phys. Rev. B,* **1998**, *57, 7027-7036.*

[37] Syzgantseva, O. A.; Calatayud, M.; Minot, C. Revealing the Surface Reactivity of Zirconia by Periodic DFT Calculations. *J. Phys. Chem. C*, **2012**, *116, 6636-6644.*

[38] Schlexer, P.; Puigdollers, A. R.; Pacchioni, G. Tuning the Charge State of Ag and Au Atoms and Clusters Deposited on Oxide Surfaces by Doping: A DFT Study of the Adsorption Properties of Nitrogen- and Niobium-Doped TiO_2 and ZrO_2. *Phys. Chem. Chem. Phys.*, **2015**, *17, 22342-22360.*

[39] Chen, H. T.; Tosoni, S.; Pacchioni, G. Adsorption of Ruthenium Atoms and Clusters on Anatase TiO_2 and Tetragonal ZrO_2 (101) Surfaces: a Comparative DFT Study. *J. Phys. Chem. C,* **2015**, *119, 10856-10868.*

[40] Zhou, F.; Zhao, X.; Xu, H.; Yuan, C. CeO_2 Spherical Crystallites: Synthesis, Formation Mechanism, Size Control, and Electrochemical Property Study. *J. Phys. Chem. C,* **2007**, *111, 1651-1657.*

[41] Bromley, S. Y.; Moreira, I. de P. R.; Neyman, K. M.; Illas, F. Approaching Nanoscale Oxides: Models and Theoretical Methods. *Chem. Soc. Rev.,* **2009**, *38, 2657-2670.*

[42] Baletto, F.; Ferrando, R. Structural Properties of Nanoclusters: Energetic, Thermodynamic, and Kinetic Effects. *Rev. Mod. Phys.,* **2005**, *77, 371-423.*

[43] Perdew, J. P.; Levy, M. Physical Content of the Exact Kohn-Sham Orbital Energies: Band Gaps and Derivative Discontinuities. *Phys. Rev. Lett.,* **1983**, *51, 1884-1887*.

[44] J. Hubbard. Electron Correlations in Narrow Energy Bands. *Proceedings of the Royal Society of London,* **1963**, *276, (1365): 238–257.*

[45] Becke, A. D. A New Mixing of Hartree–Fock and Local Density-Functional Theories. *J. Chem. Phys.* **1993**, *98, 1372-1377.*

[46] Perdew, J. P.; Burke, K.; Ernzerhof, M. Rationale for Mixing Exact Exchange with Density Functional Approximations. *J. Chem. Phys.*, **1996**, *105, 9982-9985*.

[47] Marques, M. A. L.; Vidal, J.; Oliveira, M. J. T.; Reining, L.; Botti, S. Density-based Mixing Parameter for Hybrid Functionals. *Phys. Rev. B,* **2011**, *83, 035119-035124.*

[48] Gerosa, M.; Bottani, C. E.; Caramella, L.; Onida, G.; Di Valentin, C.; Pacchioni, G. Electronic Structure and Phase Stability of Oxide Semiconductors: Performance of Dielectric-Dependent Hybrid Functional DFT, Benchmarked against *GW* Band Structure Calculations and Experiments. *Phys. Rev. B,* **2015**, *91, 155201-155216.*

[49] Kümmel, S.; Kronik, K. Orbital-Dependent Density Functionals: Theory and Applications. *Rev. Mod. Phys.,* **2008**, *80, 3-60.*

[50] Kresse, G.; Hafner, J. Ab-Initio Molecular Dynamics for Liquid Metals. *Phys. Rev. B,* **1993**, *47, 558-561*.

[51] Kresse, G.; Hafner, J. Ab-Initio Molecular-Dynamics Simulation of the Liquid-Metal–Amorphous-Semiconductor Transition in Germanium. *Phys. Rev. B,* **1994**, *49, 14251-14271.*

[52] Kresse, G.; Furthmuller, J. Efficiency of Ab-Initio Total Energy Calculations for Metals and Semiconductors using a Plane-Wave Basis Set. *Comp. Mat. Sci.,* **1996**, *6, 15-50.*

[53] Blöchl, P. E.; Projector Augmented-Wave Method. *Phys. Rev. B,* **1994**, *17953-17979.*

[54] Kresse, G.; Joubert, J.; From Ultrasoft Pseudopotentials to the Projector Augmented-Wave Method. *Phys. Rev. B,* **1999**, *59, 1758-1775.*

[55] Perdew, J. P.; Burke, K.; Ernzerhof, M. Generalized Gradient Approximation Made Simple. *Phys. Rev. Lett.,* **1996**, *77, 3865-3868.*

[56] Dudarev, S. L.; Botton, G. A.; Savrasov, S. Y.; Humphreys, C. J.; Sutton, A. P.; Electro-Energy-Loss Spectra and the Structural Stability of Nickel Oxide: An LSDA+U Study. *Phys. Rev. B,* **1998**, *57, 1505-1509.*

[57] Anisimov, V. I.; Aryasetiawan, F.; Lichtenstein, A. I. First-Principles Calculations of the Electronic Structure and Spectra of Strongly Correlated Systems: the LDA+U Method. *J. Phys.: Condens. Matter,* **1997**, *9, 767-808.*

[58] Teufer, G. The Crystal Structure of Tetragonal ZrO_2. *Acta. Cryst.,* **1962**, *15, 1187.*

[59] French, R. H; Glass, S. J.; Ohuchi, F. S.; Xu, Y. N.; Ching, E. Y. Experimental and Theoretical Determination of the Electronic Structure and Optical Properties of Three Phases of ZrO_2. *Phys. Rev. B,* **1994**, *49, 5133-5142.*

[60] Tang, W.; Sanville, E.; Henkelman, G. A Grid-Based Bader Analysis Algorithm without Lattice Bias. *J. Phys.: Condens. Matter,* **2009**, *21, 084204-084211.*

[61] Sanville, E.; Kenny, S. D.; Smith, R.; Henkelman, G. Improved Grid-Based Algorithm for Bader Charge Allocation. *J. Comput. Chem.,* **2007**, *28, 899-908.*

[62] Henkelman, G.; Arnaldsson, A.; Jonsson, H. A Fast and Robust Algorithm for Bader Decomposition of Charge Density. *Comput. Mater. Sci.,* **2006**, *36, 254-360.*

[63] Ren, X.; Rinke, P.; Blum, V.; Wieferink, J.; Tkatchenko, A.; Sanfilippo, A.; Reuter, K.; Scheffler, M. Resolution-of-Identity Approach to Hartree–Fock, Hybrid Density Functionals, RPA, MP2 and GW with Numeric Atom-Centered Orbital Basis Functions. *New Journal of Physics,* **2012**, *14, 053020-053075.*

[64] Billinge, S. J. L. The Nanostructure Problem. *Physics* **2010**, *3, 25-27.*

[65] Juhás, P.; Cherba, D. M.; Duxbury, P. M.; Punch, W. F.; Billinge, S. J. L. Ab-Initio Determination of Solide-State Nanostructure. *Nature,* **2006**, *440, 655-658.*

[66] Billinge, S. J. L.; Levin, I. The Problem with Determining Atomic Structure at the Nanoscale. *Science,* **2007**, *316, 561-565.*

[67] Neyman, K. M.; Illas, F. Theoretical Aspects of Heterogeneous Catalysis: Applications of Density Functional Methods. *Catal. Today,* **2005**, *105, 2-16.*

[68] Christiensen, A. ; Carter, E. A. First-Principles Study of the Surfaces of Zirconia. *Phys. Rev. B,* **1998**, *58, 12, 8050-8064.*

[69] Ganduglia-Pirovano, M. V.; Hofmann, A.; Sauer, J. Oxygen Vacancies in Transition Metal and Rare Earth Oxides: Current State of Understanding and Remaining Challenges. *Surf. Sci. Rep.,* **2007***, 62, 219-270*.

[70] Eichler, A.; Kresse, G. First-Principles Calculations for the Surface Termination of Pure and Yttria-Doped Zirconia Surfaces. *Phys. Rev. B* **2004**, *69, 045402-045419.*

[71] Grena, R.; Masson, O.; Portal, L.; Rémondière, F.; Berghout, A.; Jouin, J.; Thomas, P. Stabilization Effect of Surface Impurities on the Structure of Ultrasmall ZrO_2 Nanoparticles: An Ab-Initio Study. *J. Phys. Chem. C,* **2015**, *119, 15618-15626*.

[72] Zhang, F.; Jin, Q.; Chan, S. W. Ceria Nanoparticles: Size, Size Distribution, and Shape. *J. Appl. Phys.* **2004**, *95, 4319-4326*.

[73] Loschen, C.; Migani, A.; Bromley, S. T.; Illas, F.; Neyman, K. M. Density Functional Studies of Model Cerium Oxide Nanoparticles. *Phys. Chem. Chem. Phys.* **2008**, *10, 5730-5738.*

[74] Migani, A.; Neyman, K. M.; Bromley, S. T. Octahedrality Versus Tetrahedrality in Stoichiometric Ceria Nanoparticles. *Chem. Commun.,* **2012**, *48, 4199-4201*.

[75] Zaban, A.; Aruna, S. T.; Tirosh, S.; Gregg, B. A.; Mastai, Y. The Effect of Preparation Condition of TiO_2 Colloids on Their Surface Structures. *J. Phys. Chem. B,* **2000**, *104 (17), 4130-4133.*

[76] Gao, Y.; Elder, S. A. TEM Study of TiO_2 Nanocrystals with Different Particle Size and Shape. *Mater. Lett.,* **2000**, *44, 228-232.*

[77] Barnard, A. S.; Curtiss, L. A. Prediction of TiO_2 Nanoparticle Phase and Shape Transitions Controlled by Surface Chemistry. *Nano Lett.,* **2005**, *5 (7), 1261-1266.*

[78] Yudanov, I. V.; Sahnoun, R.; Neyman, K. M.; Rosch, N. J. Metal Nanoparticles as Models of Single Crystal Surfaces and Supported Catalysts: Density Functional Study of Size Effects for CO/Pd (111). *J. Chem. Phys.* **2002**, *117, 9887-9896*.

[79] Cheng, L.; Mashimo, T.; Omurzak, E.; Okudera, H.; Iwamoto, C.; Yoshiasa, A. Pure Tetragonal ZrO_2 Nanoparticles Synthesized by Pulsed Plasma in Liquid. *J. Phys. Chem. C,* **2011**, *115, 9370-9375.*

[80] Loschen, C.; Bromley, S. T.; Neyman, K. M.; Illas, F. Understanding Ceria Nanoparticles from First-Principles Calculations. *J. Phys. Chem. C Lett.,* **2007***, 111, 10142-10145.*

[81] Tsunekawa, S.; Ishikawa, K.; Li, Z. Q.; Kawazoe, Y.; Kasuya, A. Origin of Anomalous Lattice Expansion in Oxide Nanoparticles. *Phys. Rev. Lett.,* **2000**, *85, 3440-3443*.

[82] Wu, L.; Wiesmann, H. J.; Moodenbaugh, A. R.; Klie, R. F.; Zhu, Y.; Welch, D. O.; Suenaga, M. Oxidation State and Lattice Expansion of CeO_{2-x} Nanoparticles as a Function of Particle Size. *Phys. Rev. B,* **2004**, *69, 125415/1-125415/9*.

[83] W. M. Haynes. CRC Handbook of Chemistry and Physics, 96th Edition, **2015**. *CRC Press/Taylor and Francis, Boca Raton, FL*.

[84] Pacchioni, G. Oxygen Vacancy: The Invisible Agent on Oxide Surfaces. *Chem. Phys. Chem*. **2003**, *4, 1041-1047*.

[85] Huang, X.; Beck, M. J. Surface Structure of Catalytically-Active Ceria Nanoparticles. *Comp. Mat. Sci.*, **2014**, *91, 122-133*.

[86] Gallino, F.; Di Valentin, C.; Pacchioni, G. Band Gap Engineering of Bulk ZrO_2 by Ti Doping. *Phys. Chem. Chem. Phys.* **2011**, *13, 17667-17675.*

[87] Bersch, E.; Rangan, S.; Bartynski, R. A.; Garfunkel, E.; Vescovo, E. Band Offsets of Ultrathin High-κ Oxide Films with Si. *Phys. Rev. B,* **2008**, *78, 085114-085124*.

[88] Sayan, S.; Bartynski, R. A.; Zhao, X.; Gusev, E. P.; Vanderbilt, C.; Croft, M.; Banaszak-Holl, M.; Garfunkel, E. Valence and Conduction Band Offsets of a ZrO_2/SiO_xN_y/n-Si CMOS Gate Stack: A Combined Photoemission and Inverse Photoemission Study. *Phys. Status Solidi B,* **2004**, *241, 2246-2252*.

[89] Cardona, M.; Thewalt, M. L. W. Isotope Effects on the Optical Spectra of Semiconductors. *Rev. Mod. Phys.* **2005**, *77, 1173-1224*.

[90] Giustino, F.; Louie, S. G.; Cohen, M. L. Electron-Phonon Renormalization of the Direct Band Gap of Diamond. *Phys. Rev. Lett,* **2010**, *105, 265501-265505.*

Graphical Abstract